Hydroelastic Response of Lifting Bodies in Separated Multiphase Flows

Yin Lu (Julie) Young
Director, The Aaron Friedman Marine Hydrodynamics Laboratory
Professor, Department of Naval Architecture & Marine Engineering
Professor, Department of Mechanical Engineering
Professor, Department of Aerospace Engineering
University of Michigan, Ann Arbor, Michigan
UNITED STATES OF AMERICA

Email: ylyoung@umich.edu

ABSTRACT

The objective of this work is to advance the understanding of the hydroelastic response of lifting bodies in separated multiphase flows such as cavitation and ventilation. Cavitation involves phase change between liquid and vapor due to changes in the local fluid pressure; ventilation involves the transport of non-condensable gas to the submerged portion of the body without significant phase change. Both cavitation and ventilation are special forms of separated multiphase flows, and are relevant for a wide variety of marine propulsors, control surfaces, energy saving and energy harvesting devices operating at or near the free surface, or at high-speeds. Cavitation and ventilation can lead to large reduction in the mean lift/thrust, increase in drag, and cause dynamic load fluctuations, all of which can affect the vehicle performance, stability, and control authority. In addition, cavitation and ventilation can modify the local sound speed and refractive index of the fluid mixture, as well as the boundary layer and vorticity dynamics. Since many lifting devices are effectively thin plates or beams subject to high loading, flow-induced deformations may occur. These deformations/vibrations can in turn affect the surrounding multiphase flow and lead to drastically different dynamical responses compared an equivalently rigid structure. The two-way fluid-structure interactions significantly complicate the prediction, measurement, and assessment of separated multiphase flows, and may even lead to potentially catastrophic hydroelastic instabilities such as divergence, flutter, and parametric excitations. On the other hand, the fluid-structure interaction response can be tailored by taking advantage of advances in materials, sensing and control to improve the system performance, delay/control separation and multiphase flows, as well as related vibration and noise issues. In this paper, we first discuss the difference between cavitation and ventilation, and their relations to flow separation. Next, we describe the mean and unsteady hydrodynamic response of rigid lifting bodies in cavitating and ventilated flows, including the rate-dependent hysteresis response. Next, we discuss the influence of hydroelastic response on multiphase flows, the influence of multiphase flows on the hydroelastic response, and hydroelastic instabilities that can result from the two-way interactions. We will then discuss opportunities to tailor the hydroelastic response to improve performance and control multiphase flows. Finally, we will summarize current challenges associated with the prediction, measurement, and assessment of the hydroelastic response of lifting bodies in separated multiphase flows.

1.0 INTRODUCTION

Cavitation and ventilation are both special forms of separated multiphase flows, as the flow streamlines detach from the body surface because of the formation of vaporous and gaseous bubbles, respectively, which create vortices that interact with the surrounding flow. Cavitation and ventilation are relevant for a wide variety of marine lifting bodies such as propulsors, dynamic positioning devices, control surfaces, energy saving and

energy harvesting devices. Both phenomena tend to occur in regions of low pressure and low momentum such as separated flows, and in regions of high vorticity such as tip vortex. Once cavitation or ventilation incepts in the form of a small vapor- or gas-filled bubble, the bubble can quickly expand with further reduction in pressure to fill the separated region or tip vortex, and even completely replace the local liquid flow to form a large continuous vapor- or gas-filled cavity. If the cavitation or ventilation development is limited and exists only in the form of a small bubble, then it will not have a significant impact on the underlying liquid flow and resulting forces acting on the structure. However, if the cavitation or ventilation is sufficiently developed, the change in local fluid density and pressure will modify the surrounding flow dynamics and affect the forces acting on the structure. It is well known that cavitation and ventilation can lead to large reduction in mean lift/thrust, increase in drag, and cause dynamic load fluctuations, noise and vibration, all of which can affect the vessel performance, stability, and control authority. Since many lifting devices are effectively thin plates/beams subject to high loading, structural deformations and fluid-structure interaction (FSI) can come into play, which will modify and interact with the multiphase flow. The resulting complex two-way interactions introduce significant challenges to the prediction, measurement, and assessment of separated multiphase flows. Flow-induced deformations and FSI could be detrimental if not considered in the design, but they could also be advantages if intelligently tailored to improve performance and to delay/control flow separation, cavitation, and ventilation. Hence, the objective of this work is to advance the understanding of the hydroelastic response of lifting bodies in separated multiphase flows such as cavitation and ventilation.

1.1 Cavitation vs. Ventilation

Cavitation inception is caused by vaporization of the free nuclei (weak points or traveling microbubbles) in the flow when the absolute local pressure drops to below the critical pressure, which is typically assumed to be the saturated vapor pressure of the liquid [11,26]. The actual cavitation inception pressure depends on the salinity, temperature, water quality and material surface characteristics [11,26]. Cavitation can develop in different forms, including bubble cavitation, sheet cavitation, cloud cavitation, tip vortex cavitation, hub cavitation, gap cavitation, and shear cavitation. A cavity that collapses on the body surface is called a *partial cavity* (PC), while a cavity that collapses aft of the body trailing edge is called a *supercavity* (SC). A cavity that forms in the free wake of bluff bodies or in liquid jets is called a *shear cavity,* and its physics is very similar to that of tip vortex cavity [26]. A partial cavity typically undergoes periodic growing and collapse cycles, which can lead to load fluctuations, vibrations, noise, and erosion. Hence, most marine lifting bodies are designed to avoid cavitation when possible. For high-speed applications where cavitation cannot be avoided, supercavitation or artificial ventilation is typically desired to minimize cavity-induced erosion, vibration and noise by forcing the vaporous or gaseous cavity to collapse well downstream of the body trailing edge.

Ventilation involves the entrainment of predominantly non-condensable gas into submerged regions around the body. For shallowly or deeply submerged bodies, the free surface provides a readily available and continuous supply of gas, which can be drawn down to low pressure and low momentum regions (e.g. separated flow regions) around the body. Such events are called natural or *atmospheric ventilation* [36,78], and occur when there is a low energy path for air ingress to ventilation-prone regions around the body. Prior to ventilation inception, a thin layer of water, called the surface seal, separates the gas from the ventilation-prone regions on the submerged part of the body. The surface seal is a layer of unseparated flow maintained by the constant atmospheric pressure on the free surface and the flow momentum, while the low-pressure region on the body acts to draw the free surface towards the body. The thin surface seal can be breached by the growth of Taylor instabilities on the free surface [69]. Taylor instabilities are typically observed when a light fluid (e.g. air) accelerates toward a dense fluid (e.g. water), resulting in amplification of small perturbations. The growth of the small perturbations leads to the formation of aerated vortex cores that provide convenient air paths to ventilation-prone regions around the body or to a low-pressure tip vortex [59,68]. The surface seal can also be breached by

physical mechanisms such as air or water injection, or solid (debris) impingement, such that it provides a path for air ingress [34-36,78]. Previous experimental studies have shown that waves can promote ventilation of surface-piercing bodies [51]. Besides atmospheric ventilation, forced or *artificial ventilation* can also develop via the introduction of non-condensable gas by means of blowing or pumping, such as for drag reduction and flow control applications [1,26,37,50,60]. Unanticipated ventilation can lead to sudden and large changes to hydrodynamic loads, resulting in loss of vehicle control and/or lateral stability, hydroelastic instabilities (e.g. flutter, divergence, etc.), and even capsizing. For marine propulsors and dynamic positioning devices, uncontrolled ventilation can lead to rapid racing of the propellers, leading to engine damage [40,78].

1.2   Relations between Cavitation, Ventilation, and Flow Separation

Both cavitation and ventilation are strongly connected to flow separation. The separated region provides temporary shelter from the oncoming flow for the vapor or gas bubble to incept and expand in low pressure conditions. Changes to the separated region, such as flow reattachment due to transition to turbulence, can cause the bubble to be swept away. Moreover, for cases with attached turbulent boundary layer with no separation, no attached cavity can exist on the body; hence, cavitation can only appears in the form of traveling bubble cavitation originating from free nuclei carried by the flow or in the form of spot cavitation attached to isolated roughness elements [26]. Similarly, past experiments have shown that at least a very small amount of separation is necessary for an entrained gas bubble to be attached to the body surface and expand due to low surrounding pressure [13,34,35,36,68]. The interaction between cavitation/ventilation and separation can be two ways, as explosive growth of a vapor or gas bubble can trigger transition to turbulence, or replace the liquid flow altogether. The connection to separation have also motivated numerous researchers to explore methods to control cavitation/ventilation by eliminating or controlling the extent of the separated region by geometry optimization, as well as passive or active flow control strategies.

2.0   HYDRODYNAMIC RESPONSE IN SEPARATED MULTIPHASE FLOWS

In this section, we first review the steady-state and dynamic response of rigid lifting bodies in cavitating and ventilated flows. The hydroelastic response of marine lifting bodies will be presented in Section 3.0.

2.1   Hydrodynamic Response in Cavitating Flows

A key parameter that governs the hydrodynamic performance of rigid marine lifting surfaces in cavitating flows is the effective cavitation parameter, ψ:

$$\psi = \frac{\sigma}{2\alpha}; \ \sigma = \frac{P_\infty - P_c}{0.5\rho_f U^2} = \sigma_c + \frac{2}{F_{nh}^2}; \sigma_c = \frac{P_o - P_c}{0.5\rho_f U^2}; \ F_{n_h} = \frac{U}{\sqrt{gh}}; \ P_\infty = P_o + \rho g h \tag{1}$$

α is the angle of attack. σ is the classical cavitation number defined by the absolute free stream pressure P_∞ at a submerged depth of h from the free surface, the cavity pressure P_c, and the fluid dynamic pressure $0.5\rho_f U^2$. ρ_f is the fluid density, U is the inflow velocity, and g is the gravitational constant. $F_{n_h} = \frac{U}{\sqrt{gh}}$ is the submerged depth-based Froude number. In field tests and in atmospheric test facilities, $P_o = P_{atm}$. In model-scale tests where the maximum inflow or carriage speed is lower than full-scale speed, a depressurized facility (e.g. cavitation tunnel or depressurized wave basin) is typically needed to satisfy ψ similarity by lowering the absolute tunnel pressure P_o. For vaporous cavitation, P_c is equal to the saturated vapor pressure, P_v.

To illustrate the influence of ψ on the hydrodynamic performance, sample results are shown in Figs. 2-1 to 2-3 for a stainless steel (SS) hydrofoil with modified NACA 0009 cross section and a linearly tapered planform. The loaded span of the hydrofoil is $s = 0.3$ m and the mean chord is $c = 0.09$ m. The effective aspect ratio of the hydrofoil is $A_R = 2s/c$=6.7, as the foil is cantilevered at the root. The test results were obtained from the Cavitation Research Laboratory (CRL) variable pressure tunnel at the University of Tasmania with Reynolds number $\mathrm{Re} = \frac{Uc}{\nu_f} = 0.8 \times 10^6$ and $\alpha = 6^o$. Details of the experimental setup and procedure can be found in [61-64,76,77].

The variation of the ratio of the measured mean lift (C_L), drag (C_D), and moment (C_M) coefficients as a function of ψ are shown in Fig. 2-1. The symbols correspond to the mean values, and the error bars represent the amplitude of the instantaneous load fluctuations caused by unsteady cavity shedding. Sample snapshots showing leading edge partial sheet cavitation, unsteady sheet-cloud cavitation, and supercavitation are shown on the right of Fig. 2-1. The variation of the measured normalized maximum cavity length ($L_{c,max}/c$) at the foil midspan as a function of ψ is shown as symbols in Fig. 2-2. Semi-empirical equations for $C_L, C_D, C_M,$ and $L_{c,max}/c$ for hydrofoils with thin symmetric sections and $A_R > 4$ are given in Eqns. (2)-(6). The predicted values using Eqns. (2)-(6) are shown as lines in Figs. 2-1 and 2-2, which agreed well with experimental measurements. The semi-empirical equations for the Strouhal number corresponding to Type I and Type II cavity shedding frequencies are given in Eqns. (7)-(8) and will be explained next.

3-D lift coefficient

$$C_L = a_o^{3D}\alpha; \; a_o^{3D} = \frac{a_o^{2D}}{1 + \frac{a_o^{2D}}{\pi A_R}} \tag{2}$$

2-D lift slope

$$a_o^{2D} = \pi * \max\left(0.5, 2 - 5.19e^{-1.05\psi}\right) \tag{3}$$

Maximum cavity length

$$\frac{L_{c,max}}{c} = 2.326e^{-0.316\psi} \tag{4}$$

3-D moment coefficient

$$C_M = C_L e$$

$$e = \frac{e_{FW} + e_{SC}}{2} + \frac{e_{FW} - e_{SC}}{2}\tanh\frac{0.85 - L_{c,max}/c}{0.25} \tag{5}$$

$$e_{FW} = 0.25; e_{SC} = 0.05$$

3-D drag coefficient

$$C_{D,wet} = 2 \frac{0.075}{(log(Re) - 2)^2} + \frac{C_L^2}{\pi A_R};$$

(6)

$$C_D = C_{D,wet} \left(1 + 8 \frac{\psi}{s^2} e^{-\frac{\psi^2}{2s^2}} \right); \ s = 2.5$$

Type I cavity Strouhal number:

$$St_1 = \frac{f_1 c}{U} = 0.12 \text{ for } 1.2 \leq \psi \leq 3.0$$

(7)

Type II cavity Strouhal number:

$$St_2 = \frac{f_2 c}{U} = 0.0052\psi^3 + St_1$$

(8)

Cavitation first incepts in the form of bubble cavitation, which transitions to a thin leading edge partial sheet cavity at $\psi \sim 10$. Stable leading edge partial sheet cavitation transitions to unstable sheet-cloud cavitation at $\psi \sim 5$, when, the maximum cavity length at midspan is near 40% of the chord length (see Fig. 2-2). The mean C_L increases slightly with the growth of the partial cavity because of the increase in effective camber, while the amplitude of the load fluctuations increases significantly due to periodic growth and collapse of the sheet-cloud cavities. As ψ further reduces, C_L and C_M decrease, and C_D increases, until the cavity reaches near the foil trailing edge, i.e. $\frac{L_{c,max}}{c} \sim 1$, at $\psi \sim 2$. The mean C_L and C_M reach a plateau, the mean C_D decreases, and the amplitude of the load fluctuations drops drastically, when stable supercavitation develops with $\frac{L_{c,max}}{c} \geq 1.5$ at $\psi \leq 1$. As shown in Figs. 2-1 and 2-2, good general agreement is observed between measured and predicted values obtained using Eqns. (2)-(6). Nevertheless, the specific value of ψ when flow transitions between the various cavitation regimes can vary with foil geometry, and can be influenced by 3-D effects, flow unsteadiness, foil motions and deformations.

As summarized in [63,64,77], the periodic shedding of vaporous cavities have been attributed to three mechanisms: (1) growth of interfacial instabilities such as caused by formation of Kelvin-Helmholtz waves [11,10,26], (2) formation of a re-entrant jet at the rear of the cavity that moves upstream and pinches the cavity interface, allowing it to breakoff and shed downstream as a cavitating cloud/vortex [14,25,39,42,43,67,61-63], and (3) shockwave formation and propagation caused by changes in sound speed of the local fluid mixture [11,26,30,58,61-63].

Re-entrant jet driven cavity shedding are commonly referred to as *Type II oscillations* or partial cavity instability or cloud cavity instability [11,18,23,25,29,30,70]. The shedding is caused by the upstream motion of the re-entrant jet flow. As indicated in Eqn. (8), the mean-chord based Strouhal number for Type II re-entrant jet driven cavity shedding, St_2, is dependent on the maximum cavity length, and hence the effective cavitation parameter ψ [14,77]. The formation of the re-entrant jet is important for Type II shedding, as placement of a small obstacle to block the upstream motion of the re-entrant jet will modify the cavity shedding process to result in the breakup of smaller vapor structures [25]. It should be noted that re-entrant jet driven shedding of sheet-cloud cavitation tends to be the most regular and coherent regime of cavity shedding [26], and Eqn. (8) is meant to predict the dominant shedding frequency. The actual frequency response may be multi-modal, as thin cavities

tend to shed in the form of multiple small clouds rather than a single large cloud, and 3-D effects may lead to shedding of multiple clouds along the span (such as observed in the middle, right photo in Fig. 2-1) [25,61]. Moreover, for lifting bodies with non-zero sweep or skew, the direction of the re-entrant jet, which is normal to the cavity closure line, will have a spanwise component that will modify the cavity shedding dynamics [25,26]. The cavity shedding process can also appear chaotic due to interaction with shock waves generated by collapse of larger cavities with higher vapor fraction elsewhere along the body surface [61,73].
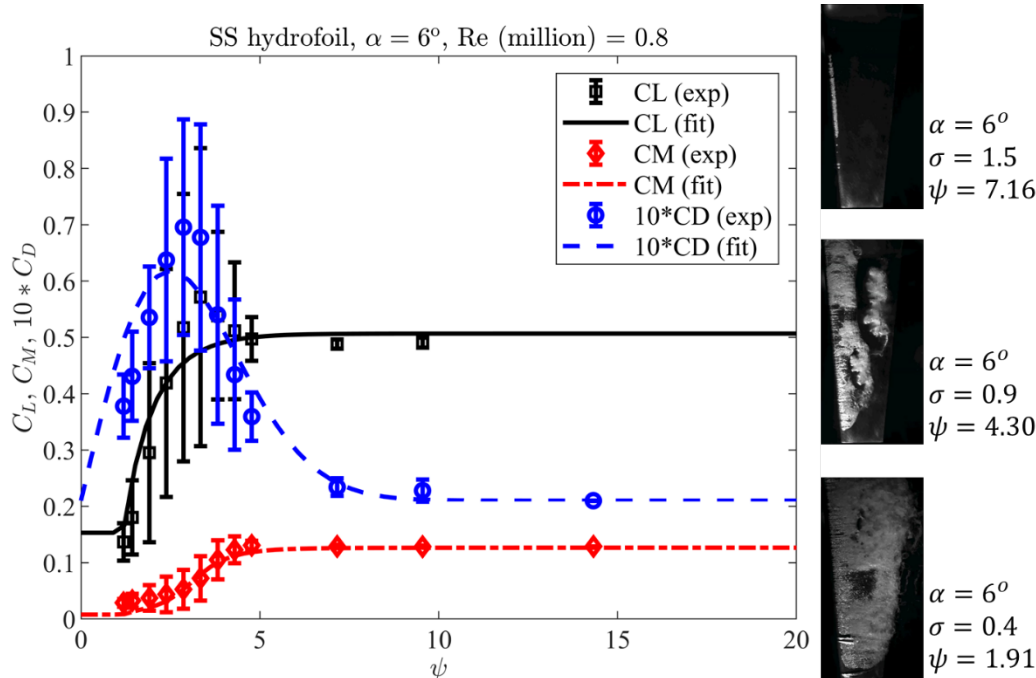

Figure 2-1: Variation of the measured mean lift (C_L), drag (C_D), and moment (C_M) coefficients as a function of the effective cavitation parameter ψ (as defined in Eqn. (1)). The symbols represent the mean values, and the error bars represent the amplitude of the instantaneous load fluctuations caused by unsteady cavity shedding. The lines represent the values predicted using Eqns. (2)-(6). Sample snapshots representing leading edge partial sheet cavitation, unsteady sheet-cloud cavitation, and supercavitation are shown on the right. All the results correspond to a SS hydrofoil with $A_R = 6.7$ at $Re = 0.8x10^6, \alpha_o = 6^o$. The experimental setup and additional results can be found in [61-64,76,77].

Shockwave-driven cavity shedding are commonly referred to as *Type I oscillations,* or transitional cavity instability [18,23,29,30,63,64,70,77]. Type I shedding is primarily driven by shockwave propagation when the local flow speed exceeds the sound speed of the liquid-vapor mixture, which typically occurs when $\frac{L_{c,max}}{c} > 0.75.$ Past experimental studies have shown that Type I oscillations yielded a near constant cavity shedding frequency of between 10-12 Hz for most hydrofoils regardless of geometry [18,23,29,63,64,70,77]. For cavities with $\frac{L_{c,max}}{c} < 0.75,$ the void fraction tends to be too low such that the speed of sound of the mixture is still higher than the local flow speed, and hence Type II re-entrant jet shedding governs. As shown in recent experimental studies, Type I and Type II cavity shedding can occur simultaneously on a lifting body or a bluff body for a limited range of effective cavitation parameters [63,64,73,77].
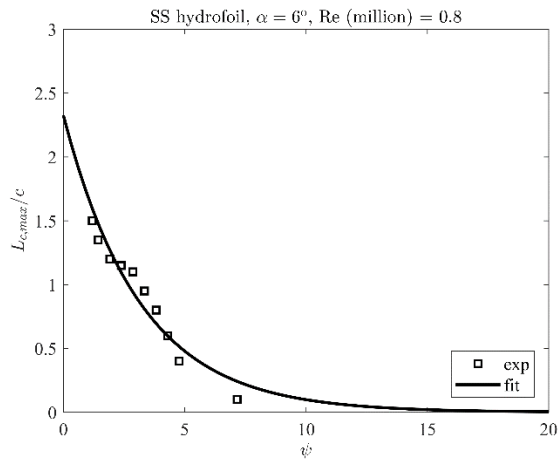
Figure 2-2: The variation of the measured normalized maximum cavity length ($L_{c,max}/c$) at the foil midspan as a function of ψ. All the results correspond to a SS hydrofoil with $A_R = 6.7$ at $Re = 0.8x10^6, \alpha = 6^o$. The graph is a replot of the results first shown in [77].
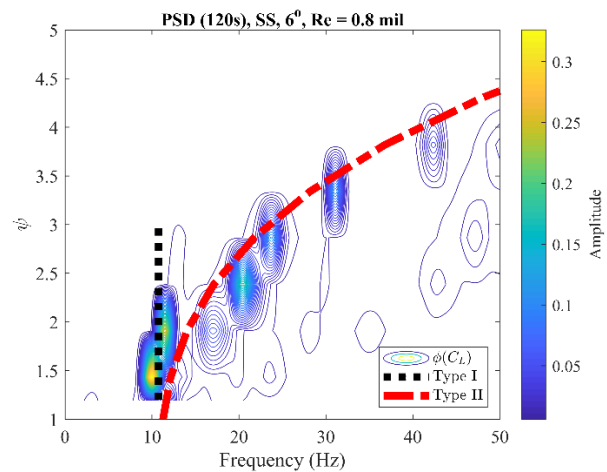
Figure 2-3: Frequency spectra of the measured instantaneous lift coefficients, along with the predicted Type I and Type II cavity shedding frequencies obtained using Eqns. (7) and (8), respectively. All the results correspond to a SS hydrofoil with $A_R = 6.7$ at $Re = 0.8x10^6, \alpha = 6^o$. The graph is a replot of the results first shown in [77].

The frequency spectra of the measured instantaneous lift coefficients for various cavitation number or ψ for the SS hydrofoil is shown as contours in Fig. 2-3, along with the predicted Type I and Type II shedding frequencies obtained using Eqns. (7) and (8), respectively. In general, the peaks of the frequency spectra fall along the predicted lines for Type I and Type II shedding. Note that the contour plot gives the appearance of isolated peaks because only a limited number of cavitation numbers were examined, and the frequency resolution was limited. Repeated measurements of the frequency response of the lift spectra with finer frequency resolution, along with post-processing of the high-speed video recordings of the same SS hydrofoil showed a more continuous band of peaks along the same Type I and Type II cavity shedding frequency curves, but also an additional higher frequency band due to secondary Type II re-entrant jet cavity shedding near the foil tip caused by 3-D effects, as well as higher frequency structural excitations [61].

In addition to cavities forming on the suction side of the body surface, cavitation can also develop behind a bluff body or a lifting body with a blunt trailing edge if the pressure drops to near the vapor pressure. As shown in recent experimental studies in [73], sufficiently high vapor fraction in the wake can lead to the formation of shockwaves, which will modify the global wake structure, including the vortex shedding frequencies and the spacing between vortices. In particular, she found that there exists two primary modes in cavitating wake flow: a sinusoidal mode that acts like a dipole caused by oscillating vortices shed from the top and bottom sides of the body trailing edge, and a pulsating mode that acts like a monopole caused by compressibility effects. The pulsating mode is responsible for increasing the shedding frequency of the cavitating wake with decreasing cavitation number until a peak develops, after which the shedding frequency decreases rapidly with further reduction in cavitation number [73]. Following the same logic, cases with artificial supercavitation (such as by injection of non-condensable gas) or fully ventilated flow should exhibit different wake dynamics because of the change in compressibility of the wake.

2.2   Hydrodynamic Response in Ventilated Flows

The hydrodynamic performance of rigid lifting surfaces in ventilated flows is also governed by the effective

cavitation parameter defined in Eqn. (1), with P_c as the cavity pressure. In the case of natural or atmospheric ventilation, $P_c = P_o$ so $\sigma_c = 0$. In the case of artificial or forced ventilation, $P_c = P_v + P_g$, where P_g is the pressure of the injected non-condensable gas, so $P_v \leq P_c \leq P_o$.

As noted in [13,34-36,59,68,72,78], there exists four primary flow regimes on a partially or shallowly submerged body: fully wetted (FW), partially ventilated (PV), partially cavitating (PC), and fully ventilated (FV) flows. Sample photographs of each of the flow regimes are shown in Fig. 2-4. Following the definitions used in [36,78], FW flow is defined as when the flow is fully wetted on both the suction and pressure sides of the body, although the separated region aft of a body with a blunt trailing edge may be base-ventilated or base-cavitating. PC and PV regimes are respectively defined as when a vaporous and a gaseous cavity are present, but does not cover the full submerged span of the body, and when the cavity is unstable because of the upstream motion of the re-entrant jet [36,78]. Cavitation and ventilation can occur simultaneously, although on different regions of a submerged body [75,34,35]. Cavitation can promote ventilation, as observed in [34,35,59,68]. Once the PC extends to beyond ~40% of the body length, the instability created by the partial cavity shedding and interactions with Taylor instabilities tend to promote transition to FV flow [35,36]. The FV regime is defined as when a stable gaseous cavity envelops the suction side of the body. It should be noted that transition from FW to FV flow can occur very rapidly, i.e. less than a second, which could lead to sudden loss of control and lateral stability, and even capsizing of the vessel, particularly at high speeds.
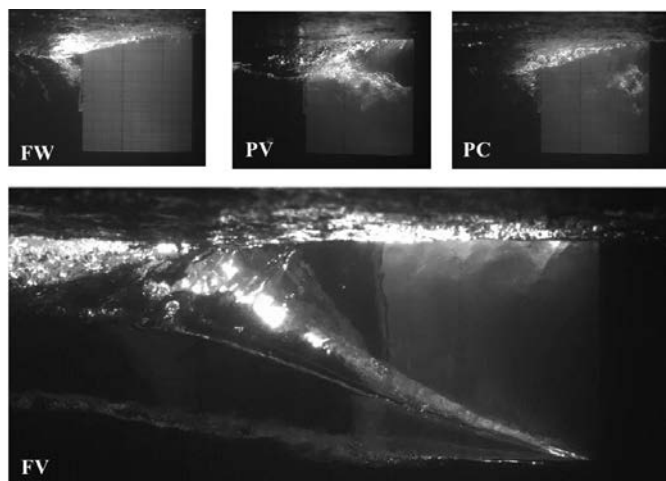

Figure 2-4: Sample snapshots of the four primary flow regimes on a surface-piercing hydrofoil: fully wetted (FW), partially ventilated (PV), partially cavitating (PC), and fully ventilated (FV) flows. Flow goes from right to left, and the free surface is at the top. See [34,36] for details about the experimental setup and results.
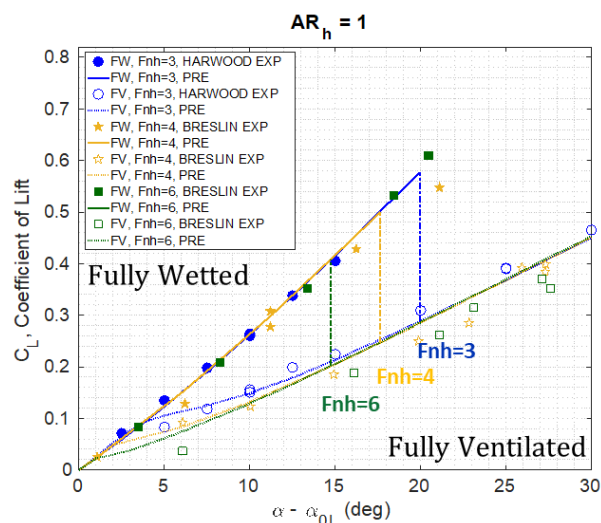

Figure 2-5: Hysteresis response of the lift coefficient as a function of α and F_{n_h} for two different surface-piercing hydrofoils with $R_h = \dfrac{h}{c} = 1$. The symbols indicate experimental data, and the lines indicate the predicted values obtained using semi-empirical relations given in [19]. The graph is taken from [19].

The dynamics between cavitation and ventilation can be very different because of the differences in compressibility between vapor and gas. Periodic shedding in PC and PV flows are driven primarily by the upstream motion of the re-entrant jet, and hence the cavity shedding frequency should depend on the cavity length, which in turn depend on ψ, like that shown in Eqn. (8). It is important to note that for partially or

shallowly submerged bodies, PC and PV flows tend to be 3-D in nature because of spanwise variations caused by pressure release at the free surface and free tip, and by hydrostatic pressure gradient effects. Consequently, the cavity length and shedding frequency will vary along the span (such as shown in Fig. 2-4), which prevents tonal frequency response caused by coherent cavity shedding. In case of atmospheric ventilation, the FV cavity tends to be stable when the turbulent cavity closure region is sufficiently downstream of the body trailing edge.

Besides atmospheric ventilation, where the gas source is from the free surface, artificial or forced ventilation by injecting gas to form/extend the cavity is a technique used for drag reduction and flow control of marine vehicles and lifting bodies [1,26,37,50,60]. The dynamics of forced ventilation depends on the cavity compliance parameter, $\frac{\sigma}{\sigma_g}$, defined in Eqn. (9), which is a measure of the relative contribution of gas to the cavity dynamics.

$$\frac{\sigma}{\sigma_g} = \frac{\sigma_v}{\sigma_g} - 1; \ \sigma_v = \frac{P_\infty - P_v}{0.5\rho_f U^2}; \ \sigma_g = \frac{P_c - P_v}{0.5\rho_f U^2}; \ \sigma = \sigma_v - \sigma_g \tag{9}$$

Note that σ_v and σ_g are respectively used to denote the cavitation number defined based on the vapor pressure and the relative pressure difference between the cavity pressure and the vapor pressure. The cavitation compliance parameter, and hence σ, is a function of the gas injection rate and F_{n_h}, which controls the form, extent, and shedding frequency of the artificial cavity. This interdependency is quite complicated, and interested readers should refer to [50,60,78] for a more extended discussion of this topic.

2.3   Rate-Dependent Hysteresis Response of Cavitating and Ventilated Flows

One particularly challenging aspect concerning the prediction, measurement, assessment, and control of cavitation and ventilation is the nonlinear rate-dependent hysteresis response, where the hydrodynamic performance depends on its history and flow speed. For cavitating flows, it is well known that the desinence cavitation parameter (the cavitation parameter at which cavitation disappears) is higher than the inception cavitation parameter because of hysteresis effect. This means that the flow speed or the angle of attack needs to be lower, or the submerged depth needs to be greater (and hence higher absolute hydrostatic pressure), than the value at cavitation inception. The same is true for ventilation. The typical rate-dependent hysteresis response of the mean lift-coefficient C_L versus angle of attack α of a surface-piercing hydrofoil is shown in Fig. 2-5, which is taken from [19]. At a given submergence depth and speed, as the angle of attack increases, the lift coefficient climbs along the FW curve until the natural ventilation develops, at which point the lift coefficient will drop rapidly. The ventilated cavity stabilizes when FV flow develops, which is when the cavity envelops nearly the entire suction surface such that the re-entrant jet flow is no longer directed upstream. Once FV, further increases in α will lead to increase in the extent of the ventilated cavity and increase in the C_L, but along the FV curve, which has a much lower slope than the FW curve. Moreover, once FV, decreases in α will cause the C_L to decrease along the FV curve until the ventilated cavity begins to wash off, which is when the re-entrant jet has an upstream component that acts to destabilize the cavity [36]. Finally, with further reduction in α, FW flow will be recovered, but at a much lower angle of attack than the ventilation inception angle. Note that for some foil geometries, α may need to be reduced to a negative value in order for the gas cavity to wash off [13]. The flow is bi-stable between the bifurcation angle, where the FW and FV curves intersect, and the natural ventilation inception angle; any external perturbation (e.g. gas, water, or debris impingement) can cause the flow to transition from FW to FV flow within the hysteresis loop. Moreover, the natural ventilation inception angle and the rewetting angle both tend to occur at lower α or lower C_L as F_{n_h} increases [19], as illustrated in Fig. 2-5. The ventilation inception angle also tends to occur earlier with decreases in the vaporous cavitation number, σ_v, i.e. when the lifting surface is operating closer to the free surface or at higher speeds. In other words, cavitation tends to accelerate ventilation inception [59,68].

3.0   HYDROELASTIC RESPONSE IN SEPARATED MULTIPHASE FLOWS

Although advances have been made in the understanding of the hydrodynamic response of separated multiphase flows, very little work has examined the hydroelastic response and stability in multiphase flows. This is because traditional marine lifting surfaces are typically made of heavy and stiff metallic alloys to withstand the high hydrodynamic loads. Consequently, the hydrodynamic and structural analyses can be decoupled, which greatly simplifies the design and analysis.   However, rigid and fixed geometry lifting surfaces suffer from performance decay when operating away from the design conditions, which can occur quite often for marine vehicles with diverse operating profiles. Given the recent interest to enhance the efficiency and reduce harmful emissions of maritime transports, lighter structures with improved performance over a wider range of operating conditions is desired.

Many advances have been made in the aerospace and wind energy industry to use advanced materials and active/passive control strategies to improve the performance of aerodynamic lifting surfaces. Examples include rotor craft and turbine blades made of anisotropic composites, which have the advantage of higher specific strength, improved damping properties, reduced electromagnetic signatures, and better fatigue characteristics compared to traditional metallic alloys [54]. Moreover, the intrinsic bend-twist and extension-twist coupling behavior of composites have been used to improve the damping, enhance stability, and reduce dynamic load variations of wings and rotor blades [27,31-33,57,66,71,74]. More recently, adaptive composite wind turbines have been shown to improve the fatigue life and overall energy capture with decreased blade loads and enhanced stall characteristics [44,45,48,49].

Composites can also be used to improve the performance of marine lifting surfaces in addition to providing the benefits of reduced weight, improved resistance to sea water corrosion, and higher damping. For marine propulsors and turbines, passive pitch adaptation through material bend-twist coupling can reduce or negate the need for large and expensive hydraulic actuators used for controllable pitch devices, thus reducing related operational and maintenance issues. Additionally, adaptive lifting surfaces are better suited for complex inflows, which is typical of marine propulsors and turbines because of the presence of the free surface, waves, currents, and interactions between hull, propulsion, and rudder. The rapid change in flow conditions coupled with the high fluid loading render most active actuation devices ineffective at high speeds. Hence, it would be desirable to take advantage of passive load-dependent shape morphing capability of anisotropic composites to improve performance. Recent experimental and numerical studies have shown that passive pitch adaptation of composite marine propeller blades can be used to delay and/or reduce cavitation, and increase fuel-efficiency, compared to their rigid counterparts when operating at off-design conditions and/or non-uniform inflows [79]. Similar advantages have been found numerically for marine turbines [8,52,55], where adaptive blades were shown to improve performance, reduce structural loads, and reduce or delay cavitation. Nevertheless, most of the past work did not consider the dynamic response and stability in multiphase flow. Hence, the objective of this section is to summarize recent research on the two-way interactions between hydroelastic deformations of lifting surfaces and multiphase flows.

3.1   Influence of Hydroelastic Response on Multiphase Flows

The interplay between elastic body deformation and multiphase flows was studied in [2-4,9,12,15,16,21,22,61-64,76,77,80-82]. In general, the studies showed that deformations that yield nose-up twist, which will increase the effective angle of attack, lead to higher hydrodynamic loads, accelerated flow separation and stall, earlier cavitation/ventilation inception, longer cavities, and lower cavity shedding frequencies compared to a rigid hydrofoil with the same unloaded geometry. The opposite is true for deformations that lead to nose-down twist [3,5,6,76-79,82].

To illustrate, sample results are shown in Fig. 3-1 for the cavitating response of three hydrofoils with identical unloaded geometry: one stainless steel (SS) hydrofoil and two composite hydrofoils. The SS hydrofoil is the same as described in Section 2.1, where the results are shown in Figs. 2-1 to 2-3. The two composite hydrofoils are both made of epoxy resin reinforced with the same nominal layup of carbon fiber reinforced polymers (CFRP) and glass fiber reinforced polymers (GFRP). The only difference between the two composite hydrofoils is the orientation of the structural CFRP layers, which are oriented +30º and -30º from the spanwise axis for the P30 and N30 hydrofoils, respectively. The fiber orientation is defined positive towards the foil leading edge. All three hydrofoils were tested in the in the same cantilevered configuration with the same mounting and setup at the Cavitation Research Laboratory variable pressure tunnel at the University of Tasmania. Details of the experimental setup and procedure can be found in [61-64,82,76,77].
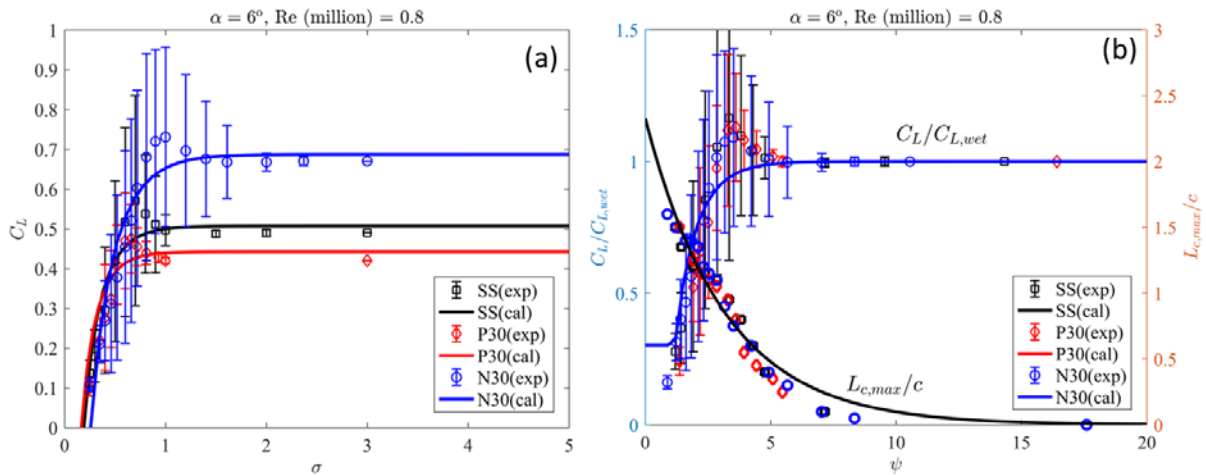
Figure 3-1: (a) Variation of the measured lift coefficient (C_L) against the cavitation number (σ) for three hydrofoils with identical unloaded geometry and setup. **(b)** Variation of the measured lift coefficients normalized by their respective fully wetted values ($C_{L,wet}$), and the measured normalized maximum cavity length ($L_{c,max}/c$), against the effective cavitation parameters ($\psi = \sigma/2\alpha_{eff}$) for all 3 hydrofoils, where $\alpha_{eff} = \alpha_o + 2\theta_{tip}/\pi$ with θ_{tip} as the tip twist angle in FW flow. Also shown in solid lines are the predicted values using Equation (2)-(4). θ_{tip} is equal to 0º, -1.2º, and +3.36º for the SS, P30, and N30 hydrofoils, respectively, at $Re = 0.8x10^6, \alpha_o = 6^o$. Graphs taken from [76].

The results shown in Fig. 3-1 are taken from [76] for $Re = \frac{Uc}{v_f} = 0.8 \times 10^6$ and $\alpha = 6^o$ for varying cavitation numbers, σ. The plot on the left of Fig. 3-1 shows that the mean C_L for the N30 and P30 hydrofoils are respectively higher and lower than the SS hydrofoil in FW flow, i.e. when $\sigma > 3$. The corresponding measured tip twist angle, θ_{tip}, for the SS, P30, and N30 hydrofoils are respectively 0º, -1.2º, and +3.36º in FW flow at $Re = 0.8x10^6, \alpha_o = 6^o$. Nose-up twist is defined as positive. Compared to the SS hydrofoil, the fluctuations in C_L is observed at higher values of σ, which is indicative of earlier cavitation inception, for the N30 hydrofoil because of the nose-up twist. For the same reason, the normalized maximum cavity lengths ($L_{c,max}/c$) are longer for the N30 hydrofoil compared to the SS hydrofoil at the same σ and α. Conversely, the P30 hydrofoil exhibited delayed cavitation inception and shorter cavity length compared to the SS hydrofoil because of the nose-down twist.

The plot on the right of Fig. 3-1 show that the normalized lift coefficient relative to the mean FW values, $C_L/C_{L,wet}$, and the normalized maximum cavity lengths, $L_{c,max}/c$, at the midspan for all three hydrofoils can be collapsed on the same trend lines when plotted against $\psi = \frac{\sigma}{2\alpha_{eff}}$, where $\alpha_{eff} = \alpha_o + \frac{2\theta_{tip}}{\pi}$ is the effective angle of attack. α_o is the geometric angle of attack and θ_{tip} is the tip twist angle in FW flow. θ_{tip} was not measured in cavitating flow because of challenges associated with flow-induced vibrations. The $2/\pi$ factor for θ_{tip} is used to account for the spanwise variation in twist, which is assumed to take the shape of a half sine curve, which goes from zero at the root to θ_{tip} at the tip. The lines in Fig. 6 correspond to the predicted values using the semi-empirical relations shown in Eqns. (2)-(8) by replacing α with α_{eff}. Good general agreement is observed between predictions and measurements.

Comparisons of the observed cavitation patterns of the SS, P30, and N30 hydrofoils are shown in Fig. 3-2 along with the predicted cavitation patterns obtained by using Eqns. (2)-(4). To obtain the 3-D cavitation patterns, we assumed elliptic loading distribution, and the local 2-D or sectional effective angle of attack is defined as $\alpha_{eff}(y) = \alpha_o + \theta(y) + \alpha_i(y)$. $\theta(y)$ is the twist angle at spanwise coordinate y. $\alpha_i(y)$ is negative and is the induced angle of attack caused by the 3-D downwash. The predicted spanwise variation of the Type I and Type II cavity shedding frequencies obtained using Eqns. (7)-(8) with $\alpha_{eff}(y)$ are shown on the bottom of Fig. 3-2. The contour of the measured frequency spectra of the instantaneous lift coefficient for the P30 and N30 hydrofoils across a range of σ values are shown in Fig 3-3; the corresponding contour for the SS hydrofoil is shown in Fig. 2-3. The predicted Type I and Type II cavity shedding frequencies are shown as black dashed lines and red dashed-dotted lines, respectively, in Figs. 2-3 and 3-3.

As shown in Fig. 3-2, the cavity extent is longer, and the Type II re-entrant jet cavity shedding frequency is lower, for the N30 hydrofoil because of the nose-up twist compared to the SS hydrofoil for the same flow condition. The opposite is true for the P30 hydrofoil. In addition, while only Type II re-entrant jet shedding is predicted for the SS and the P30 hydrofoils, Type I shockwave driven shedding is also predicted for the N30 hydrofoil because ψ is low enough with the increase in α_{eff} such that the vapor volume fraction is high enough for shockwaves to form. For all 3 hydrofoils, the peaks are much more intense for the Type I shockwave driven cavity shedding compared to the Type II re-entrant jet cavity shedding. This is probably because the Type II cavity shedding frequency varies along the span with the cavity length, and hence not coherent, compared to the Type I cavity shedding frequency, which is constant at ~11 Hz throughout most of the span.

In general, the peaks of the lift frequency spectra fall along the predicted Type I and Type II cavity frequency curves in Figs. 2-3 and 3-3. The peaks of the Type II re-entrant jet cavity shedding have much lower amplitude for the P30 and N30 hydrofoils than the SS hydrofoil. This is probably because composite hydrofoils have higher damping. For the P30 hydrofoil, there is a strong peak near 32 Hz, which is suspected to be due to lock-in of the Type II cavity shedding frequency with the harmonic of the Type I shockwave driven cavity shedding frequency and with the fundament natural frequency of the P30 hydrofoil in supercavitating (SC) conditions. As shown in Fig. 3-2, the cavity is collapsing just aft of the trailing edge for the N30 hydrofoil at $\alpha_o = 6^o$ and $\sigma = 0.6$, where both Type I and Type II cavity shedding mechanisms are present. At 32 Hz, the Type II re-entrant jet cavity shedding frequency is nearly three times the Type I shockwave cavity shedding frequency. Moreover, although the FW natural frequency of the N30 hydrofoil is near 30 Hz, the SC natural frequency is higher because of reduction in added mass caused by replacement of water with vapour on the suction side. The combined effect is believed to be responsible for the high intensity peak near 32 Hz, which was audible during the experiment.
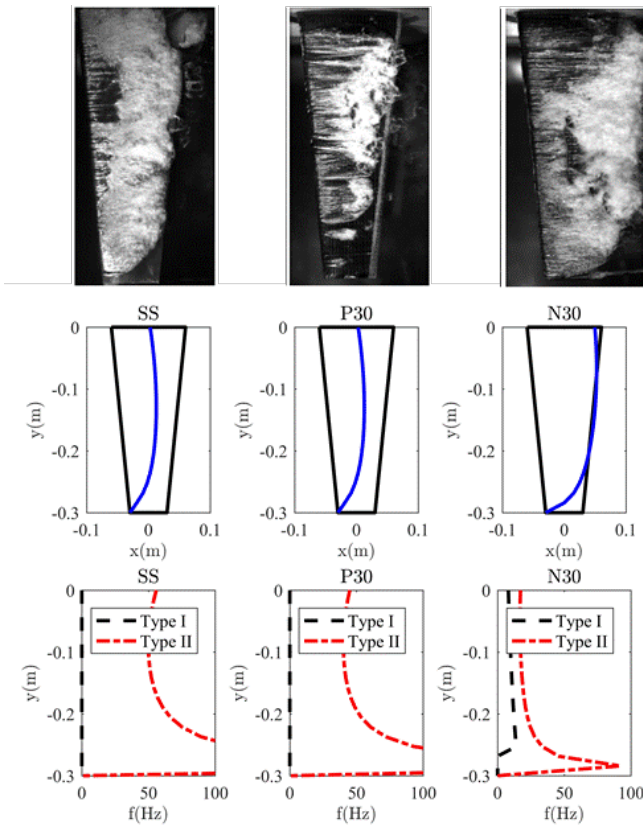
Figure 3-2: Comparisons of the observed (top) and predicted (middle) cavitation patterns, and the predicted Type I and Type II cavity shedding frequencies (bottom), obtained using Eqns. (2)-(8) with $\psi = \sigma/2\alpha_{eff}$, for the SS, P30, and N30 hydrofoils at $Re = 0.8x10^6, \alpha_o = 6^o$, and $\sigma = 0.6$. Graphs taken from [76].
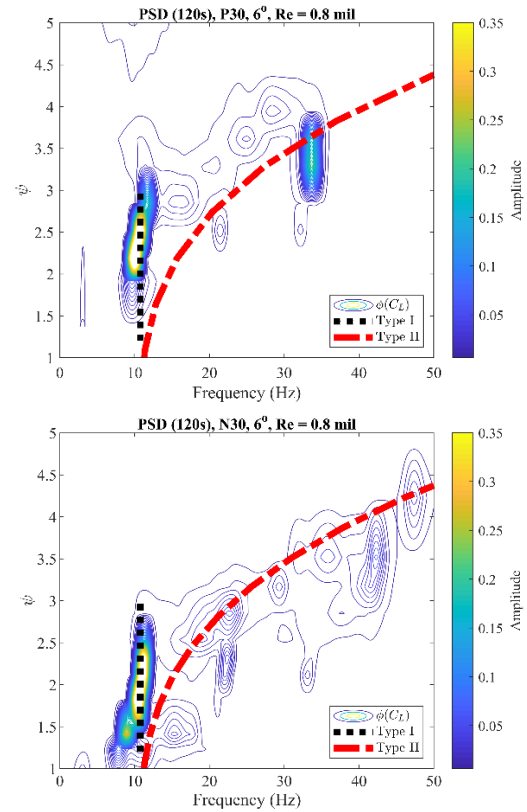
Figure 3-3: Contour of the frequency spectra of the measured instantaneous lift coefficients for the P30 (top) and N30 hydrofoil (bottom), along with the predicted Type I and Type II cavity shedding frequencies obtained using Eqns. (7) and (8), respectively, with $\psi = \sigma/2\alpha_{eff}$, $Re = 0.8x10^6, \alpha = 6^o$. The graphs are replotted based on the data first shown in [76].

## 3.2   Influence of Multiphase Flows on Hydroelastic Response

As evident via the results shown in Figs. 3-1 to 3-3, the hydroelastic response affects the multiphase flow, and the resulting loads acting on the structure. In turn, the multiphase flow also affects the hydroelastic response. Previous experimental and numerical studies showed that the natural frequencies of partially submerged or shallowly submerged bodies decreases with increasing immersion because of increase in fluid added mass [28,34,35,41,47,53,81]. Moreover, the ratio of the wet-to-dry frequencies depend on the mode shape because the fluid inertial forces vary with the displacement direction. The system natural frequencies and damping coefficients also vary with flow speed because the fluid forces vary with flow speed, and the effect is more apparent for lightweight marine structures because of the lower solid-to-fluid added mass ratio [5,6,15,16,20,35]. In addition, the presence and increasing extent of cavitation and ventilation will tend to increase the natural frequencies because of reduction in added mass caused by water being displaced by much lighter vapor and gas, respectively [2,4,35,81].

The influence of the flow conditions on the natural frequencies of a surface-piercing hydrofoil is shown in Fig. 3-4. The hydrofoil has a rectangular planform with uniform cross sections, and was cantilevered from the top. The hydrofoil is made of PVC with a thin Aluminum strip (0.6 cm thick $\times$ 2.79 cm wide) affixed to the blunt trailing edge (TE) to increase the bending rigidity for sustained testing. The span is s=0.914 m and the chord is c=0.279 m. The submerged depth of the hydrofoil is h, and the submerged aspect ratio is $AR_h = \frac{h}{c}$. The experimental studies were conducted at (1) the Physical Model Basin (PMB) at the Aaron Friedman Marine Hydrodynamics Laboratory (MHL) at the University of Michigan in Michigan, USA, and (2) the free surface variable pressure recirculating water channel at the Italian National Research Council - Institute of Marine Engineering (CNR INM) in Rome, Italy. Details of the experimental setup and results can be found in [34-36]. Sample flow patterns for the reinforced PVC hydrofoil with $AR_h = 1$ are shown in Fig. 2-4.
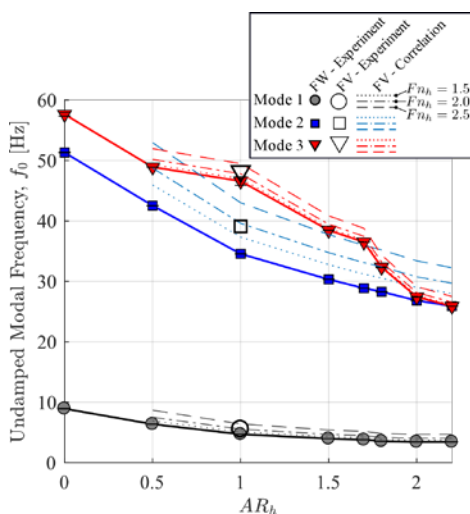
Figure 3-4: Variation of the measured FW undamped modal frequencies in quiescent fluid (in solid lines and filled symbols) for varying immersed aspected ratio, AR_h, for a reinforced PVC surface-piercing hydrofoil. Also shown are the measured FV modal frequencies for $AR_h = 1$ in open circles, and the extrapolated FV modal frequencies for varying AR_h and F_{n_h} in dashed lines. Graph taken from [81].
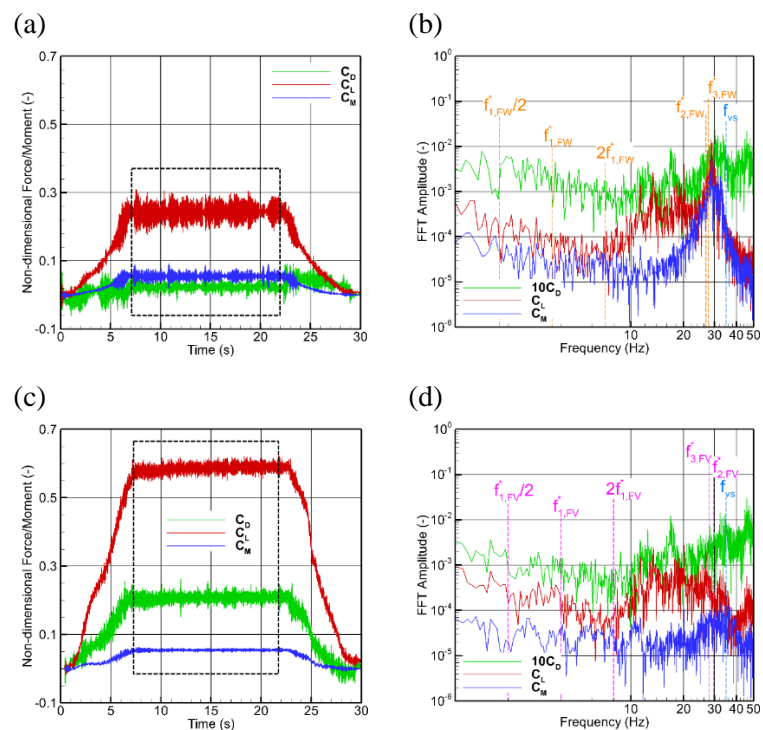
Figure 3-5: Measured time histories and frequency spectra of C_D, C_L, and C_M of the reinforced PVC hydrofoil at α = 5° in FW flow in (a) and (b), respectively, and at α = 20° in FV flow in (c) and (d). All cases are for AR_h = 2.0 and Fn_h = 1.5 in calm water conditions. Graph taken from [81].

The measured 1st mode is bending, the 2nd mode is twisting, while the 3rd mode is the 2nd bending with some twisting. $AR_h = 0$ corresponds to the dry condition. In general, the natural frequencies decrease with increasing submerged aspect ratio, AR_h. For $2 \le AR_h \le 2.2$, the natural frequencies for modes 2 and 3 coalesced in FW and quiescent condition. Although towing tank studies did show a slight dependence of the natural frequencies with forward speed, the change was small because the maximum speed was limited to 6.2 m/s [34,35,81]. As shown in Fig. 3-4, the natural frequencies are higher in FV flow compared to FW flow, and the frequencies for modes 2 and 3 separated in FV flow at $AR_h = 2$.

The significance of frequency coalescence is illustrated in Fig. 3-5. The measured time histories and frequency spectra of the lift, drag, and moment coefficients (C_L, C_D, and C_M) at $\alpha = 5^\circ$ in FW flow are shown in Figs. 3-5(a) and 3-5 (b), respectively. Similar results for $\alpha = 20^\circ$ in FV flow are shown in Figs. 3-5 (c) and 3-5 (d). All the cases in Fig. 3-5 are for $AR_h = 2.0$ and $Fn_h = 1.5$ in calm water conditions, and have been shown in [81]. Based on the complex flow dynamics in FV conditions, one would expect the load fluctuations relative to the mean value to be higher in FV flow than in FW flow. However, the opposite is observed in Fig. 3-5. This is because of dynamic load amplification caused by coalescence of modes 2 and 3 in FW flow (as evident via Fig. 3-5(b). In FV flows, modes two and three separated (as shown in Fig. 3-5(d)) because of changes in added mass caused by ventilation, which lead to significant reduction in amplitude of the dynamic load fluctuations compared to FW flow. Similar conclusions were observed for the measured time histories and frequency response of the tip deformations [81]. A more detailed presentation of the results will be presented in an upcoming paper by the author [80].

As shown in Figs. 3-4 and 3-5, ventilation changes the modal characteristics, and hence dynamic hydroelastic response. Similar observations were made in the response of flexible hydrofoils in unsteady cavitating flows via experimental and numerical studies presented in [2,4,63,64]. These studies show that unsteady cavitation leads to temporal variations in the fluid inertial, damping, and de-stiffening forces, which leads to modification and modulation of the frequency response. In turn, the elastic foil deformations modified the cavity dynamics. As illustrated in [2,4,63,64], the Type II re-entrant cavity shedding frequency for a flexible hydrofoil can deviate significantly from the rigid values, and instead lock-in to the foil fundamental natural frequency, its harmonics or subharmonics due to parametric excitations.

3.3   Hydroelastic Instabilities in Multiphase flows

As outlined in the examples above, two-way interactions between multiphase flow and structural deformations can lead to flow-induced vibrations and even hydroelastic instabilities. Resonance is an externally excited instability, which occurs when the external excitation frequency (e.g. propeller rotation frequency, engine excitation frequency, or wave excitation frequency) matches with one of the system natural frequencies. Flutter is a self-excited instability that occurs when the system damping of one of the modes goes to or below zero. The natural frequencies and damping coefficients vary with speed and operating condition because of changes in the fluid added mass, damping, and de-stiffening force, which are components of the fluid force in phase with the structural acceleration, velocity, and displacement. Experimental measurements of the changes in the generalized fluid forces with speed and with the cavitation and ventilation, as well as resulting change in natural frequencies and damping coefficients can be found in [35]. Periodic growth and collapse of unsteady cavitation/ventilation will further add to the periodic fluctuations of the system parameters. The resulting temporal change in the system mass, damping, and stiffness properties will lead to parametric excitations. In addition to modulation of the system natural frequencies, the change in the system damping can lead to instabilities. Flutter is one example where the flow feeds energy to further drive the structural vibrations. Parametric resonance can also develop when the cavity modulation frequency is near a multiple of the parametric excitation frequency, which will result in exponential growth of the oscillation amplitudes and eventual material failure, as demonstrated in the numerical study presented in [4].

In addition to dynamic instabilities, static instability in the form of static divergence can also develop when the deformations grow without bounds because of loss in effective stiffness caused by the fluid de-stiffening force exceeding the structural elastic restoring force. Experimental and numerical studies by [2,3,22,34,35] suggested that cavitation and ventilation tend to delay static divergence due to reduction in the mean lift and moment, but may instead accelerate flow-induced vibrations and flutter. In addition, recent numerical studies [5-6] showed that a new low-frequency bending-dominated mode (also called divergence root or divergence mode) can

emerge at high speeds. The emergence of the new mode is because of the memory term in the unsteady fluid loads caused by the shed vortices in the wake, which has a damping component that grows with $\rho_f U$ and a fluid de-stiffening component that grows with $\rho_f U^2$. This new mode can lead to single-mode flutter when the damping of this new mode drops to zero. The emergence of this new mode and single-mode flutter have been observed for strut-pod systems in water [5,9], and for aircraft wings [24], but it can occur more readily (and at much lower speeds) for lightweight lifting bodies in water [5-6,38]. In addition, the new mode can lead to earlier divergence when both the frequency and damping of this new mode goes to zero, while the frequencies of the original structural modes (modes that exists in vacuum) are still positive. This type of divergence can be dangerous, as it can happen with little warning and it only develops at sufficiently high speeds [38].

## 4.0   TALORING THE HYDROELASTIC RESPONSE IN MULTIPHASE FLOWS

In the previous section, we illustrated the complex two-way interactions between the hydodroelastic response and multiphase flows. The results illustrated how the hydroelastic response can change the multiphase flow, including the impact on separation, stall, cavitation and ventilation. We also illustrated how multiphase flows can in turn modify the system vibration characteristics, which will lead to different dynamical response compared to an equivalent rigid structure, and may even lead to hydroelastic instabilities. The objective of this section is to illustrate how the hydroelastic response can be tailored to control flow-induced vibrations and avoid hydroelastic instabilities in multiphase flow.

For a given geometry, the flow-induced excitation frequencies of a rigid lifting body caused by vortex or cavity shedding can be determined by using semi-empirical relations such as presented in Eqns. (2)-(8), or via experimental and numerical studies. The external flow excitation frequencies such as caused by wind, waves, propeller, etc. can also be determined. Hence, the next step in the design process is to select and design the material and structure to avoid dynamic load amplifications and hydroelastic instabilities. This can be conducted using a coupled FSI solver that can predict the variation of the system modal characteristics with flow conditions. Note that the modal characteristics and instability mechanisms can be very different between in-air and in-water operations. This was already demonstrated in Fig. 3-4 for a reinforced PVC surface-piercing hydrofoil. To show another example and to illustrate how the material can be tailored to affect the dynamic response, comparisons of the measured dry and wet modal frequencies of cantilevered composite hydrofoils with varying Carbon-UD angles (ϕ) are shown in Fig. 3-6. Similar trends were predicted using high-fidelity and low fidelity coupled FSI solvers in [46] and [5], respectively. All the hydrofoils have the same unloaded geometry and are made of the same material, as explained in Section 2.1. As illustrated in Fig. 3-6, the natural frequencies vary with ϕ, which implies that the foil natural frequencies can be tailored by changing ϕ, without any changes to the structural geometry or material. The structure can be designed such that the natural frequencies are well separated from each other and from the flow excitation frequencies. However, such tailoring should be conducted using the in-water modal frequencies, as they are substantially different than the in-air values, as illustrated in Fig. 3-6.
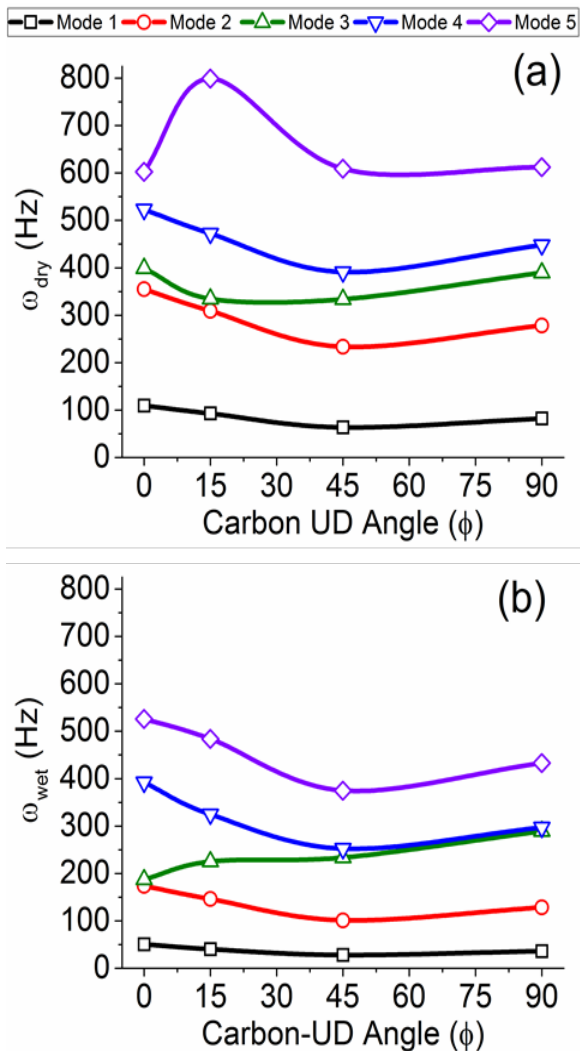
Figure 3-6: Influence of the Carbon-UD angle on the measured dry (a) and wet (b) natural frequencies of composite hydrofoils with identical unloaded geometry in quiescent fluid. Graph taken from [56].
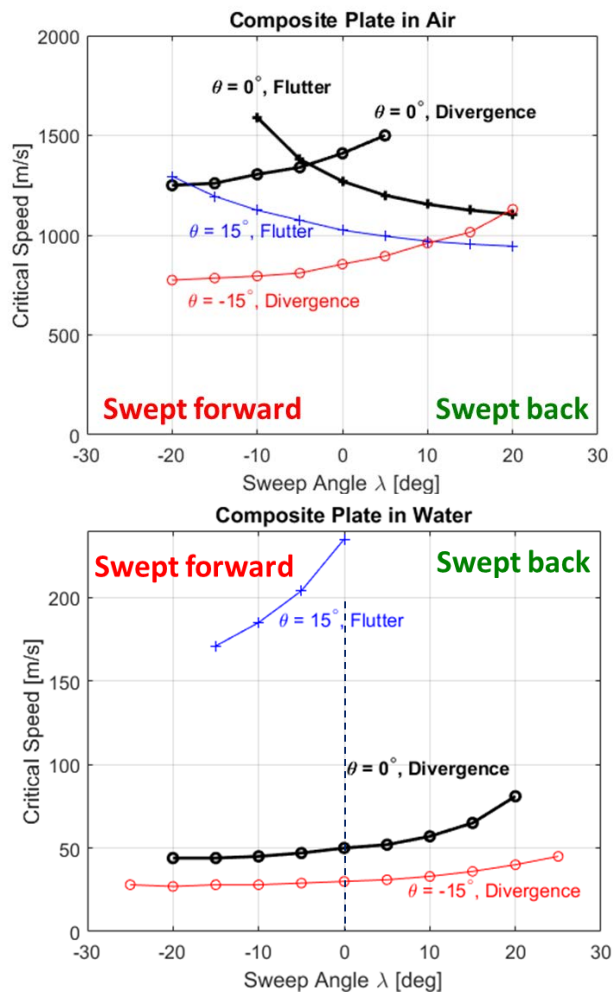
Figure 3-7: Influence of fiber orientation angle (θ) and sweep angle (λ) on the static divergence and flutter boundaries of composite plates in air (top) and in water (bottom). All the results assumed the cantilevered CFRP plate to be 30 cm long, 10 cm wide, and 1.2 cm thick in fully attached flow. Graph taken from [6].

To avoid hydroelastic instabilities, the critical speed boundaries must be known, which again are very different between in-air and in-water operations and can only be predicted using a coupled FSI solver. Examples of the predicted static divergence and flutter boundaries of CFRP plates in-air and in-water for varying fiber orientation angle (θ) and sweep angle (λ) are shown in Fig. 3-7. The critical speeds are generally much lower in water compared to in air. This is because the fluid loads are much higher in water, where the density is about 1000 times higher than air. For the composite plate in air, the highest critical speed corresponds to a foil with a forward sweep of $\lambda = -5^o$ and the fibers aligned along the spanwise direction ($\theta = 0^o$). For the plate in water, a backward swept hydrofoil ($\lambda > 0^o$) with fibers aligned toward the inflow ($\theta > 0^o$) is needed to avoid divergence and flutter.

Figures 3-1 to 3-5 demonstrated how the mean and unsteady hydrodynamic response, cavitation pattern and cavity shedding frequencies, can changed by tailoring the material. Figures 3-6 and 3-7 showed how the system vibration frequencies and hydroelastic stability boundaries can be modified by tailoring the material. These results suggest that there is an opportunity to passively tailor the hydroelastic response of lifting bodies in multiphase flow by taking advantage of advances in materials and the understanding of the FSI response. In addition, it is also possible to use active strategies to control multiphase flow. Recent experimental studies by [35] discovered that ventilation formation and elimination can be controlled by applying very small amplitude excitation forces (less than 5% of the lift) at the modal frequencies. In particular, the excitation of the first bending mode in water was found to encourage ventilation inception, while excitation of higher order bending and twisting modes was found to encourage ventilation washout and rewetting. More research is needed to develop sensing and control strategies to actively control multiphase flow and hydroelastic response. Research is also needed to study the interactions between elastic modes of lifting surfaces and rigid body modes of high-speed marine vehicles, where body-freedom flutter [17,24] and other system instabilities can develop.

5.0   SUMMARY & FUTURE WORK

The objective of this work is to advance the understanding of the hydroelastic response of lifting bodies in separated multiphase flows, with focus on cavitating and ventilated conditions. We first summarized the differences between cavitation and ventilation, and their relations to flow separation in Section 1. In Section 2, we summarized how cavitation and ventilation affect the mean and unsteady hydrodynamic response of rigid lifting bodies in cavitating and ventilated flows, including the rate-dependent hysteresis response. In Section 3, we reviewed the influence of hydroelastic response on multiphase flows, the influence of multiphase flows on the hydroelastic response, and hydroelastic instabilities that can result from two-way FSI. In Section 4, we demonstrated how the system modal characteristics and hydroelastic stability boundaries of composite hydrofoils can be tailored by adjusting the fiber orientation angle or sweep angle. We also explained how small excitations can be applied to control the inception and washout of multiphase flows. Although we have improved our understanding of the hydroelastic response and stability of lifting bodies in separated multiphase flows, much more work is still needed to better understand the complex interplay between structural deformations and multiphase flows and associated potential hydroelastic instabilities. To do so, we need to advance our current ability to predict, measure, and assess the hydroelastic response in multiphase flows.

5.1   Current Challenges and Future Work

One of the current challenges to measurement and assessment is the ability to perform time-synchronized measurements of the velocity and void fraction distribution of multiphase flow over rigid and flexible bodies. Such information is needed to determine the detailed interplay between boundary layer development, flow separation, cavitation, ventilation, structural deformations and vibrations. It is a challenge because the refractive index is modified in the presence of cavitation or ventilation, which challenges optical measurement techniques, and the problem is made even more complicated by structural deformations and vibrations. Only recently were researchers able to measure the void fraction of the flow mixture using x-ray densitometry, which lead to the important finding that shockwave formation and propagation is an important driver of cavitation collapse in addition to re-entrant jet formation and propagation [73]. Moreover, cavitation and ventilation can occur in the form of a discrete bubble(s), many interacting bubbles, or as one large continuous bubble, all of which can change spatially and temporally in the flow. Moving fluid-solid interfaces create another challenge. However, recent advances in 3-D flying shape sensing [34,35] or motion capturing systems, and Digital Image Correlation techniques [56], can be used to measure the structural dynamics.

Another challenge in measurement and assessment of cavitation and ventilation is their stochastic nature. For example, the inception of tip vortex cavitation requires the chance encounter of a free cavitation nucleus with the moving tip vortex. Hence, the probability of cavitation inception depends on the size and density distribution of cavitation nuclei in the flow, as well as flow conditions that govern the size, strength, and movement of the tip vortex. Needless to say, the problem gets more complicated if the structure is moving or deforming. Similar problems exist for ventilation, as atmospheric ventilation inception is often triggered by chance encounters with flow disturbances that break the surface seal to provide low energy paths for air ingress. Hence, the flow tends to transition more readily from fully wetted to fully ventilated states in full-scale because of the rough sea surface, while such transition would be delayed in laboratory conditions with calm water surface, leading to much more explosive type of transitions [59] and different structural responses. In addition, transition to turbulence, cavitation and ventilation inception all depend on the background turbulence level, which can be very different between laboratory and full-scale conditions.

Prediction of the hydroelastic response in separated multiphase flows can be even more daunting. The flow solver must be able to correctly capture the temporal and spatial evolution of the various fluid phases with very different density, viscosity, and compressibility. It is also challenging to predict the dynamic change between the discrete and continuous forms of multiphase flow, and its dependence on nuclei size and density distribution, as well as background turbulence. The simultaneous existence of cavitation and ventilation, the complex transitions between the various flow regimes, and the history-dependent nature of the hysteresis response all post significant challenge to currently available flow prediction methods. The problem is made even more complicated by the need to consider the constitutive material behaviour, the FSI response, and potential hydroelastic instability and material failure mechanisms.

Prediction, measurement, and assessment of the hydroelastic response in multiphase flow are also complicated by the many non-dimensional parameters that may influence the system response. The Froude number is the ratio of flow inertial force to gravitational force, which affects the susceptibility to cavitation and ventilation, as well as the trajectory of the vapor or gas filled bubbles. The Reynolds number is the ratio of flow inertial force to viscous force, which affects the development of the wall boundary layer and flow separation, and hence cavitation and ventilation. In addition, viscosity affects the cavitation inception pressure. The Weber number is the ratio of the flow inertial force to surface tension force, which affects the strength of the surface seal, the structure of surface sprays, and the pressure difference between inside and outside of the bubble, all of which can affect cavitation and ventilation inception. The Mach number is the ratio of flow speed to the sound speed of the fluid mixture, and governs the relative importance of compressibility effects, which influence the collapse dynamics of cavitation bubbles and subsequent interaction with adjacent bubbles, vortices, and material surface. Water quality affects the size and distribution of cavitation nuclei, which in turn affects the susceptibility to cavitation inception. The surface roughness can affect the boundary layer development by triggering transition to turbulent and encouraging the growth of the boundary layer, which will in turn affect the inception and stability of cavitation and ventilation. Temperature can affect heat transfer at the interface, and hence bubble growth rate and collapse dynamics. The heat generated by the collapse of cavitation bubble may increase or accelerate material damage. The combination of all of these effects make scaling cavitation and ventilation much more challenging than just satisfying similarity in ψ.

In addition to all the parameters that affect the multiphase flow, there are additional parameters that affect the material and fluid-structure interaction response. The steady-state hydroelastic response and stability is governed by the Cauchy number, which is the ratio of the elastic restoring force to fluid disturbing force. For anisotropic material and 3-D structures, geometric similarity and kinematic similarity are also needed, which requires the material/structural bend-twist and extension-twist coupling to be the same between the model and the prototype. The problem is even more challenging for dynamic hydroelasticity problems, as the ratio of the

fluid-to-solid inertial, damping, and stiffness forces to be the same between the model and the prototype, which can make it extremely challenging, if not impossible, to find suitable model-scale materials that satisfy all the similarity requirements [78,79]. Even if a material could be found such that the static and dynamic hydroelastic similarity conditions are met, the material failure mechanisms and failure loads are likely to be different and cannot be scaled. Hence, multiple scaled model tests and numerical simulations may be needed to examine the various scaling effects.

The above brief summary outlines the current challenges associated with the prediction, measurement, and assessment of the hydroelastic response of lifting bodies in separated multiphase flows. Such advances are needed to improve our understanding of the governing physics and to develop innovative means to take advantage of advances in materials and manufacturing, sensing and control to improve system performance, delay/control cavitation/ventilation, minimize flow-induced vibrations and noise, avoid hydroleastic instabilities, and enable in situ flow and structural health monitoring.

ACKNOWLEDGEMENTS

REFERENCES

[1]   Acosta, A.J., 1973. Hydrofoils and Hydrofoil Craft. *Annual Review of Fluid Mechanics*, 5(1):161-184.

[2]   Akcabay, D.T., Chae, Young, Y.L., Ducoin, A., and Astolfi, J.A., 2014. Cavity-induced vibration of flexible hydrofoils. *Journals of Fluids and Structures*, 49: 463-484.

[3]   Akcabay, D.T. and Young, Y.L., 2014. Influence of cavitation on the hydroelastic stability of hydrofoils. *Journals of Fluids and Structures*, 49: 170-185.

[4]   Akcabay, D.T. and Young, Y.L., 2015. Parametric excitations and lock-in of flexible hydrofoils in two-phase flows. *Journal of Fluids and Structures*, 57: 344-356.

[5]   Akcabay, D.T. and Young, Y.L., 2019a. Steady and dynamic hydroelastic behavior of composite lifting surfaces. *Composite Structures*, under review.

[6]   Akcabay, D.T. and Young, Y.L., 2019b. Material anisotropy and sweep angle effects on flexible lifting-surfaces in water compared to in air. *Composite Structures*, under preparation.

[7]   Ausoni, P., Farhat, M., Escaler, X., Egusquiza, E., and Avellan, F., 2007. Cavitation influence on von Karman vortex shedding and induced hydrofoil vibrations. *Journal of Fluids Engineering*, 129(8): 966–973.

[8]   Barber, R., and Motley, M., 2016. Cavitating response of a passively controlled tidal turbine blade. *Journal of Fluids and Structures*, 66: 462–475.

[9]   Besch, P.K. and Liu, Y. N., 1974. Hydroelastic design of subcavitating and cavitating hydrofoil strut

systems. *Report No. AD-780 776.* Naval Ship Research and Development Center, Maryland, USA.

[10] Brandner, P.A., Walker, G.J., Niekamp, P.N., and Anderson, B., 2010. An experimental investigation of cloud cavitation about a sphere. *Journal of Fluid Mechanics*, 656: 147-176.

[11] Brennen, C.E., 1995. Cavitation and bubble dynamics. *Oxford University Press*. New York, NY, USA.

[12] Brennen, C., Oey, K. T., and Babcock, C. D., 1980. Leading-edge flutter of supercavitating hydrofoils. *Journal of Ship Research*, 24(3):135–146.

[13] Breslin, J. P. and Skalak, R., 1959. Exploratory study of ventilated flows about yawed surface-piercing struts. *Techical Report 2-23-59W. NASA,* Washington, DC, USA.

[14] Callenaere, M., Franc, J., Michel, J., and Riondet, M., 2001. The cavitation instability induced by the development of a re-entrant jet. *Journal of Fluid Mechanics,* 444: 223-256.

[15] Chae, E.J., Akcabay, D.A., Lelong, A., Astolfi, J.A., and Young, Y.L., 2016. Numerical and experimental investigation of natural flow-induced vibrations of flexible hydrofoils. *Physics of Fluids*, 28: 075102.

[16] Chae, E.J., Akcabay, D.A., and Young, Y.L., 2017. Influence of flow-induced bend–twist coupling on the natural vibration responses of flexible hydrofoils. *Journal of Fluids and Structures,* 69: 323-340.

[17] Chen, G.-S. and Dugundji, J., 1987. Experimental aeroelastic behavior of froward-swept graphite/epoxy wings with rigid-body freedom. *Journal of Aircraft,* 24(7): 454-464.

[18] Coutier-Delgosha, O., Devillers, J.F., Pichon, T., Vabre, A., Woo, R. and Legoupil, S., 2006. Internal structure and dynamics of sheet cavitation. *Physics of Fluids,* 18: 017103.

[19] Damley-Strnad, A., Harwood, C. and Young, Y.L., 2019. Hydrodynamic performance and hysteresis response of hydrofoils in ventilated flows. *Sixth International Symposium on Marine Propulsors (SMP'19)*, Rome, Italy.

[20] Dehkharqani, A.S., Aidanpää, J.O., Engström, F. and Cervantes, M.J., 2018. A review of available methods for the assessment of fluid added mass, damping, and stiffness with an emphasis on hydraulic turbines. *Applied Mechanics Review*, 70(5).

[21] Ducoin, A., Astolfi, J. A., and Gobert, M., 2012. An experimental study of boundary-layer transition induced vibrations on a hydrofoil. *Journal of Fluids and Structures*, 32: 37–51.

[22] Ducoin, A. and Young, Y.L., 2013. Hydroelastic response and stability of a hydrofoil in viscous flow. *Journal of Fluids and Structures*, 38: 40-57.

[23] Duttwiler, M. E. and Brennen, C.E., 2002. Surge instability on a cavitating propeller. *Journal of Fluid Mechanics*, 458: 133-152.

[24] Edwards, J. and Wieseman, C., 2008. Flutter and divergence analysis using the generalized aeroelastic analysis method. *Journal of Aircraft,* 45(3): 906-915.

[25] Franc, J.P., 2001. Partial cavity instabilities and re-entrant jet. *Fourth International Symposium on Cavitation (CAV 2001)*, California Institute of Technology, Pasadena, CA USA.

[26] Franc, J. and Michel, J., 2004, Fundamentals of cavitation. *Dordrecht: Kluwer Academic Publishers*.

[27] Friedmann, P., Venkatesan, C., and Yuan, K., 1992. Development of a structural optimization capability for the aeroelastic tailoring of composite rotor blades with straight and swept tips. *4th AIAA Symposium on Multidisciplinary Analysis and Optimization*.

[28] Fu, Y. and Price, W.G. 1987. Interactions between a partially or totally immersed vibrating cantilever plate and the surrounding fluid. *Journal of Sound and Vibration*, 118(3): 495-513.

[29] Fujii A., Kawakami, D.T., Tsujimoto, Y. and Arndt, R.E.A., 2007. Effect of hydrofoil shapes on partial and transitional cavity oscillations. *Journal of Fluids Engineering*, 129: 669-673.

[30] Ganesh, H., Makiharju, S.A., and Ceccio, S.L., 2016. Bubbly shock propagation as a mechanism for sheet-to-cloud transition of partial cavities. *Journal of Fluid Mechanics*, 802: 37-78.

[31] Ganguli, R., and Chopra, I., 1997. Aeroelastic tailoring of composite couplings and blade geometry of a helicopter rotor using optimization methods. *Journal of American Helicopter Society*, 42(3): 218–228.

[32] Glaz, B., Friedmann, P., and Lu, L., 2009. Helicopter vibration reduction throughout the entire flight envelope using surrogate-based optimization. *Journal of American Helicopter Society*, 54(1): 012007.

[33] Green, J., 1987. Aeroelastic tailoring of aft-swept high-aspect-ratio composite wings. *Journal of Aircraft*, 24: 812–819.

[34] Harwood, C.M., Felli, M., Falchi, M., Ceccio, S.L., and Young, Y.L., 2019a. The Hydroelastic Response of a Surface-Piercing Hydrofoil in Multi-phase Flows: Part I – Passive Hydroelasticity. *Journal of Fluid Mechanics*, under review.

[35] Harwood, C.M., Felli, M., Falchi, M., Garg, N., Ceccio, S. L., and Young, Y.L., 2019b. The Hydroelastic Response of a Surface-Piercing Hydrofoil in Multi-phase Flows: Part II – Modal Parameters and Generalized Fluid Forces. *Journal of Fluid Mechanics*, under review.

[36] Harwood, C.M., Young, Y.L., and Ceccio, S.L., 2016. Ventilated cavities on a surface-piercing hydrofoil at moderate Froude numbers: cavity formation, elimination, and stability. *Journal of Fluid Mechanics,* 800: 5-56.

[37] Hecker, R. and Ober, G., 1974. Flow separation, reattachment, and ventilation of foils with sharp leading edge at low reynolds number. *Report no. AD-787500*, Naval Ship Research and Development Center, Maryland, USA.

[38] Heeg, J., 2000. Dynamic investigation of static divergence: analysis and testing. *Report No. TP-2000-210310*. NASA, Hampton, VA, USA.

[39] Kawanami, Y., Kato, H., Yamaguchi, H., Tanimura, M., and Tagaya, Y., 1997. Mechanism and control of

cloud cavitation. *Journal of Fluids Engineering*, 119 (4): 788-794.

[40] Koushan, K., Spence, S. J. B., and Hamstad, T., 2009. Experimental Investigation of the Effect of Waves and Ventilation on Thruster Loadings. *First International Symposium on Marine propulsors*, Trondheim, Norway.

[41] Kramer, M.R., Liu, Z., and Young, Y.L., 2013. Free vibration of cantilevered composite plates in air and in water. *Composite Structures*. 95: 254-263.

[42] Laberteaux, K. R. and Ceccio, S. L., 2001a. Partial cavity flows. Part 1 -- cavities forming on models without spanwise variation. *Journal of Fluid Mechanics*. 431: 1-41.

[43] Laberteaux, K. R. and Ceccio, S. L. 2001b., Partial cavity flows. Part 2 -- cavities forming on test objects with spanwise variation. *Journal of Fluid Mechanics*. 431: 43-63.

[44] Lackner, M., and Rotea, M., 2010. "Passive structural control of offshore wind turbines". Wind Energy, 14(3): 373–388.

[45] Lee, A., and Flay, R., 2000. Compliant blades for passive power control of wind turbines. *Wind Engineering,* 24: 3–11.

[46] Liao, Y., Garg, N., Martins, J.R.R.A., and Young, Y.L., 2019. Viscous fluid structure interaction response of composite hydrofoils. *Composite Structures*, 212: 571-585, 2019.

[47] Lindholm, U.S., Kana, D.D., Chu, W.H., and Abramson, H.N., 1965. Elastic Vibration Characteristics of Cantilever Plates in Water. *Journal of Ship Research.* 9: 11-22.

[48] Lobitz, D., and Veers, P., 2003. Load mitigation with bending/twist-coupled blades on rotors using modern control strategies. *Wind Energy*, 6: 105–117.

[49] Maheri, A., and Isikveren, A., 2009. Performance prediction of wind turbines utilizing passive smart blades: approaches and evaluation. *Wind Energy*, 13: 255–265.

[50] Mäkiharju, S. and Ceccio, S.L., 2018. On multi-point gas injection to form an air layer for frictional drag Reduction. *Ocean Engineering*, 147: 206-214.

[51] McGregor, R.C., Wright, A. J., Swales, P.D., and Crapper, G.D., 1973. An examination of the influence of waves on the ventilation of surface-piercing struts. *Journal of Fluid Mechanics,* 61(1): 85.

[52] Motley, M., and Barber, R., 2014. Passive control of marine hydrokinetic turbine blades. *Composite Structures*, 110: 133–139.

[53] Motley, M.R., Kramer, M.R., and Young, Y.L., 2013. Free surface and solid boundary effects on the free vibration of cantilevered composite plates. Composite Structures**,** 96: 365-375.

[54] Mouritz, A., Gellert, E., Burchill, P., and Challis, K., 2001. Review of advanced composite structures for naval ships and submarines. *Composite Structures*, 53: 21–41.

[55] Nicholls-Lee, R., Turnock, S., and Boyd, S., 2013. Application of bend-twist coupled blades for horizontal axis tidal turbines. *Renewable Energy*, 50: 541–550.

[56] Phillips, A.W., Cairns, R.C., Davis, P., Norman, P., Bradner, P.A. Pearce, B.W. and Young, Y.L., 2017. Effect of material design parameters on the forced vibration response of composite hydrofoils in air and in water. *Fifth International Symposium on Marine Propulsors (SMP 17)*, Espoo, Finland.

[57] Popelka, D., Parham, T., Lindsay, D., Berry, V., and Baker, D., 1995. Results of an aeroelastic tailoring study for a composite tiltrotor wing. *Annual Forum Proceedings-American Helicopter Society*, 2: 1117–1131.

[58] Reisman, G.E., Wang, Y.C. & Brennen, C.E., 1998. Observations of shock waves in cloud cavitation. *Journal of Fluid Mechanics*, 355: 255-283.

[59] Rothblum, R.S., Mayer, D.A. and Wilburn, G.M., 1969. Ventilation, Cavitation and other Characteristics of High Speed Surface-Piercing Strut. *Technical Report 3023.* Naval Ship Research and Development Center, Washington, DC, USA.

[60] Semenenko, V.N., 2001, Artificial supercavitation, physics and calculation. RTO AVT Lecture Series on Supercavitating Flows (2001), Brussels, Belgium.

[61] Smith, S.M., Venning, J.A., Brandner, P.A., Pearce, B.W., Giosio, D.R., and Young, Y.L., 2018. The influence of fluid-structure interaction on cloud cavitation about a hydrofoil. *10th International Symposium on Cavitation (CAV2018)*. Baltimore, Maryland, USA.

[62] Smith, S.M., Venning, J.A., Giosio, D.R., Brandner, P.A., Pearce, B.W., and Young, Y.L., 2019a. Cloud cavitation behavior on a hydrofoil due to fluid-structure interaction. *Journal of Fluids Engineering*, 141: 041105.

[63] Smith, S.M., Venning, J.A., Pearce, B.W., Young, Y.L., and Brandner, P.A., 2019b. The influence of fluid-structure interaction on cloud cavitation about a stiff hydrofoil (Part 1). *Journal of Fluid Mechanics*, under review.

[64] Smith, S.M., Venning, J.A., Pearce, B.W., Young, Y.L., and Brandner, P.A., 2019c. The influence of fluid-structure interaction on cloud cavitation about a flexible hydrofoil (Part 2). *Journal of Fluid Mechanics*, under preparation.

[65] Song, C.S. 1969. Vibration of cavitating hydrofoils. *Lab Project Rept. No. 111.*, St. Anthony Falls Hydraulic Laboratory, Minneapolis, MN, USA.

[66] Soykasap, O., and Hodges, D., 2000. Performance enhancement of a composite tilt-rotor using aeroelastic tailoring. *Journal of Aircraft*, 37: 850–858.

[67] Stutz, B. and Reboud, J.L., 1997. Experiments on unsteady cavitation. *Experiments in Fluids*, 22 (3): 191-198.

[68] Swales, P.D., Wright, A.J., McGregor, R.C. and Rothblum, R., 1974. The Mechanism of Ventilation Inception on Surface Piercing Foils. *Journal of Mechanical Engineering Science*, 16(1): 18–24.

[69] Taylor, G.T., 1950. The Instability of liquid Surfaces when accelerated in a direction perpendicular to their planes. *Proceedings of the Royal Society A: Mathematical, Physical and Engineering Sciences*, 201(1065):192-196.

[70] Tsujimoto, Y., Watanabe, S., and Horiguchi, H., 2008. Cavitation instabilities of hydrofoils and cascades. *International Journal of Fluid Machinery and Systems*, 1(1): 38-46.

[71] Weisshaar, T.A. and Foist, B.L., 1985. Vibration tailoring of advanced composite lifting surfaces. *Journal of Aircraft,* 22(2): 141-147.

[72] Wright, A., Swales, P.D. and McGregor, R.C., 1972. Ventilation inception on surface piercing foils or struts. *Nature*, 240(5382): 465-466.

[73] Wu, J., 2019, Bubbly shocks in separated cavitating flows. *Ph.D. Dissertation*. University of Michigan, Ann Arbor, Michigan, USA.

[74] Yamane, T., 1992. Aeroelastic tailoring analysis for advanced turbo propellers with composite blades. *Computers and Fluids*, 21: 235–245.

[75] Young, Y.L. and Brizzolara, S., 2013. Numerical and physical investigation of a surface-piercing hydrofoil. *3rd International Symposium on Marine Propulsors (SMP'13)*, Launceston, Tasmania, Australia.

[76] Young, Y.L., Garg, N., Brandner, P.A., Pearce, B.W., Clarke, D., and Philips, A.W., 2018a. Load-dependent bend-twist coupling effects on the steady-state hydroelastic response of composite hydrofoils. *Composite Structures*. 189: 398-418.

[77] Young, Y.L., Garg, N., Brandner, P.A., Pearce, B.W., Butler, D., Clarke, D., and Philips, A.W., 2018b, Material bend-twist coupling effects on cavitating response of composite hydrofoils. *10th International Cavitation Symposium (CAV2018)*, Baltimore, MD, USA.

[78] Young, Y.L., Harwood, C.M., Montero, F.M., Ward, J.C., and Ceccio, S. L., 2017. Ventilation of lifting surfaces: review of the physics and scaling relations. *Applied Mechacnis Reviews*, 69(1).

[79] Young, Y.L., Motley, M. R., Barber, R.B., Chae, E., and Garg, N., 2016. Adaptive Composite Marine Propulsors and Turbines: Progress and Challenges. *Applied Mechacnis Reviews*, 68(6).

[80] Young, Y.L., Wright, T., Yoon, H., and Harwood, C.M., 2019. Dynamic hydroelastic response of a surface-piercing strut in waves and ventilated Flows. *Journal of Fluids and Structures*, under preparation.

[81] Young, Y.L., Yoon, H., Wright, T., and Harwood, C.M., 2018c. The effect of waves on ventilation on the dynamic response of a surface-piercing hydrofoil. *32nd Symposium on Naval Hydrodynamics*, Hamburg, Germany.

[82] Zarruk, G.A., Brandner, P.A., Pearce B.W., and Phillips, A.W., 2014. Experimental study of the

steady fluid–structure interaction of flexible hydrofoils. *Journal of Fluids and Structures*, 51: 326-343.